Special Section: Noninvasive Imaging of Processes in Natural Porous Media

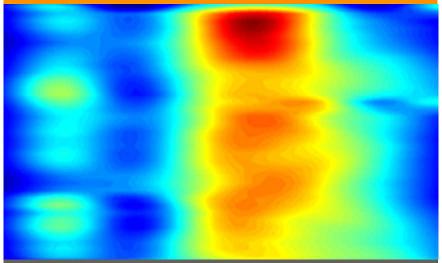

Magnetic Resonance Monitoring and Numerical Modeling of Soil Moisture during Evaporation

Steffen Merz,* Bruce J. Balcom, Razieh Enjilela, Jan Vanderborght, Youri Rothfuss, Harry Vereecken, and Andreas Pohlmeier

Evaporation from bare soil surfaces can be restrained to a great extent with the development of a dry layer at the soil surface where capillary hydraulic conductance ceases and water flow proceeds only by gas phase transport. Model calculations and preliminary experiments with model porous media have shown that this surface layer can be very thin. An accurate characterization of these processes is required, which is provided by noninvasive magnetic resonance (MR) methods. The evaporative drying of a silt loam and a sandy loam was monitored at high spatial resolution in laboratory experiments. The MR data were used to assess the performance of two numerical models: (i) the Richards equation, which considers isothermal liquid water flow, and (ii) a coupled soil water, heat, and vapor flow numerical model. The experimental results reveal two distinct drying regimes for both soil types where, at the onset of the second evaporation stage, a dry surface zone developed with increasing thickness over time. This layer revealed that water loss inside the soil coincided with a relatively low evaporation rate as the liquid continuity to the soil surface vanished. The modeling results clearly demonstrated the need to consider heat and vapor flow. It was shown, as a proof of principle, that MR relaxation time spectra may serve as a proxy to follow desaturation processes where spatially resolved transverse relaxation can reveal a secondary evaporation front.

Abbreviations: CPMG, Carr–Purcell–Meiboom–Gill; MR, magnetic resonance; NMR, nuclear, magnetic resonance; NSE, Nash–Sutcliffe coefficient of efficiency; rf, radio frequency; SE-SPI, spin echo single-point imaging; SPRITE, single-point ramped imaging with longitudinal relaxation time enhancement.

Evaporation from water surfaces (e.g., oceans and streams), from soil surfaces, and plant transpiration constitute components in the terrestrial water cycle because they deplete more than half of all precipitation (Oki and Kanae, 2006). Evaporation from bare soil surfaces consumes one quarter of the incoming solar radiation and therefore controls the vapor and energy fluxes from the groundwater to the atmosphere (Trenberth et al., 2009). Because soils typically consist of a solid phase and voids that are filled by liquid and gas phases in different fractions, they are natural porous media. The drying of soil, without a supplying water reservoir, usually proceeds in two distinct stages (Or et al., 2013; Scherer, 1990; Schlünder, 2004).

During the first stage (S1), the water potential at the soil surface is sufficiently high and the vapor pressure in the gas phase of the porous medium is close to the saturated vapor pressure. If the evaporation rate is not too high, the vapor pressure of the surface air layer is in equilibrium with the saturated vapor pressure in the porous medium and the evaporation rate is close to that of a free water surface, e_{pan}. Therefore, the evaporation rate during S1 is determined by the evaporative demand of the atmosphere and is often referred to as the energy-limited stage. During this stage, the evaporative demand is supplied by the hydraulically connected capillary water flow from within the porous medium to the surface, where the transition to vapor occurs. The process at this stage is controlled and determined by external conditions such as net radiation, vapor pressure deficit (Ben Neriah

Core Ideas

- Evaporative drying of soil columns was monitored in high resolution using NMR.
- Soil moisture data were used for validating a water, vapor, and heat flow model.
- The Richards approach was insufficient under Stage II conditions.
- NMR is a feasible technique for soil moisture measurements under Stage II conditions.

S. Merz, J. Vanderborght, Y. Rothfuss, H. Vereecken, and A. Pohlmeier, Agrosphere (IBG-3), Institute of Bio- and Geosciences, Forschungszentrum Jülich GmbH, 52425 Jülich, Germany; S. Merz, Fundamental Electrochemistry (IEK-9), Institute of Energy and Climate Research, Forschungszentrum Jülich GmbH, 52425 Jülich, Germany; B.J. Balcom and R. Enjilela, Dep. of Physics, MRI Research Centre, Univ. of New Brunswick, Fredericton, NB, Canada. *Corresponding author (s.merz@fz-juelich.de).

Received 20 Oct. 2016.
Accepted 25 Sept. 2017.

Citation: Merz, S., B.J. Balcom, R. Enjilela, J. Vanderborght, Y. Rothfuss, H. Vereecken, and A. Pohlmeier. 2018. Magnetic resonance monitoring and numerical modeling of soil moisture during evaporation. Vadose Zone J. 17:160099. doi:10.2136/vzj2016.10.0099

et al., 2014), and wind velocity (Shahraeeni et al., 2012). During S1, the desaturation of the soil surface decreases the matric pressure head, which causes upward water flow from deeper, wetter layers. However, when the surface dries further and the liquid water potential becomes negative, the equilibrium vapor pressure in the gas phase that is in contact with the liquid phase becomes significantly smaller than the saturated vapor pressure so that the evaporation rate decreases below that of a free water surface. In this case, the evaporation rate depends also on the flow and transport properties of the porous medium, which determine the water potentials and vapor pressures at the soil surface. When the surface becomes very dry and the hydraulic conductivity is very low, vapor pressure and water potential at the soil surface are determined by the transport of vapor in the gas phase and the evaporation occurs below the surface inside the porous medium at a secondary evaporation front.

With ongoing evaporation, this front recedes downward, leading to a larger transport distance or diffusive path length for vapor between the secondary evaporation front and the soil surface. Consequently, the evaporation rate decreases with time. This is the second stage of drying (S2). Various approaches for the prediction of the onset of S2, the extent of the dry surface layer, and the evaporation rate during S2 can be found in the literature (e.g., van Keulen and Hillel, 1974; Laurindo and Prat, 1998; Lehmann et al., 2008; Or et al., 2013; Qiu and Ben-Asher, 2010; Yiotis et al., 2007). A comprehensive approach to describe the coupled heat, vapor, and liquid transport in porous media was introduced by Philip and De Vries (1957). Nevertheless, predicting drying rates and moisture development in soils remains challenging, particularly under S2 conditions (Tran et al., 2015).

The standard approach to simulate vertical soil moisture profiles is the one-dimensional Richards equation, which considers isothermal water flow but neglects vapor transport in the soil. The upper boundary condition at the soil surface is the potential evaporation as prescribed flux during S1 until a critical water potential is reached, which is used as a constant pressure head boundary during S2. Because vapor transport in the porous medium is not considered in the Richards equation, the evaporation plane remains at the soil surface; therefore, this equation does not reproduce a dried surface layer above an evaporation plane that recedes within the porous medium through which water transfer occurs by vapor diffusion (Jassal et al., 2003; Zeng, 2013). Therefore, to compute vertical moisture profiles that reproduce a dried layer on top of an evaporation plane, the water flow needs to be coupled to vapor and heat fluxes (Liu et al., 2005; Novak, 2010; Sakai et al., 2009; Teng et al., 2016). In addition to the vertical soil moisture profiles, the soil temperature profiles are affected by the location of the evaporation plane, where energy is transformed into latent heat. When the evaporation plane is below the soil surface, the absorbed radiation energy at the soil surface must be transferred by heat conduction into the porous medium toward the evaporation plane, where it is transferred into latent heat. Therefore, a retreat of the evaporation plane into the porous medium leads to stronger heating of the soil surface than if the evaporation plane is pinned to the soil surface, as assumed in the Richards equation. Neglecting the emergence of a dried surface layer may therefore have important consequences when evaporation rates are estimated from surface temperature measurements that are obtained with remote sensing (Qiu and Ben-Asher, 2010; Robinson et al., 2008). Several studies on evaporation from bare soils have been conducted for the lysimeter and mesoscale (Assouline et al., 2013; Bittelli et al., 2008; Dimitrov et al., 2015; Jassal et al., 2003; Liu et al., 2005; Moghadas et al., 2013, 2014; Vanderborght et al., 2010; Wythers et al., 1999).

Although the evaporation process is relevant for a water balance in fields and hydrological catchments and although there are several recent studies focusing on the observation or estimation of evaporation fluxes at these scales, the process is controlled by transfer processes in the thin surface soil layer. Therefore, there is a need to develop noninvasive methods for investigating the development of the dry surface layer and processes within it. In a first step, these methods can be developed and tested in the laboratory (e.g., Han and Zhou, 2013; Shokri et al., 2008). Noninvasive studies related to S2 evaporation at the laboratory scale have been conducted by Rothfuss et al. (2015) using stable isotope measurements. Heitman et al. (2008) developed sensors that can measure heat flux profiles in detail and thus determine the location of the evaporation front. Moghadas et al. (2013) investigated the sensitivity of ground-penetrating radar measurements to the development of a drying front, and Merz et al. (2014) monitored the drying process of a sand column by means of different magnetic resonance (MR) methods. Merz et al. (2015b) used a unilateral MR instrument to monitor the near-surface moisture content in a laboratory lysimeter filled with natural silt loam to show that this method would be applicable in the field and is not restricted to a laboratory setting.

Since MR was first used for the determination of soil moisture by Andreev and Martens (1960), the technique and associated methods have undergone constant improvement, and MR has become a versatile toolkit in the field of environmental science (Nestle et al., 2007), particularly for porous media research (Koptyug, 2012). Magnetic resonance is preferred over other methods used for monitoring moisture because it is noninvasive and provides information on the environment of the water and insights into the diffusion pathways of water molecules in a probed volume (Korb, 2011; Watson and Chang, 1997). Direct field application of MR has become possible since the concept of single-sided or unilateral MR has become more manageable (Casanova, 2011; Kleinberg and Jackson, 2001).

In a preceding study (Merz et al., 2015a), we tested several MR imaging methods with respect to their potential for moisture determination with high resolution in the upper thin soil layer. The present work complements these experimental observations of the drying of two different soil materials with simulations by the classical Richards model and by a model that considers liquid water, vapor, and heat fluxes and proves the principle of MR. In addition, we investigated the potential of spatially resolved relaxometry to determine the thickness of the dry layer.

Theory

All moisture measurements were performed by means of ^{1}H magnetic resonance (MR), which is solely sensitive to the signal from the H atoms in H_2O. The resulting ^{1}H-MR signal is thus a measure of the amount of liquid H (water) in the system, where the signal additionally depends on the water environment (pores) (Dunn et al., 2002). The moisture content was monitored by means of (i) the Carr–Purcell–Meiboom–Gill (CPMG) method, which uses an echo train whereby the signal amplitude is interpolated to $t = 0$, and (ii) the Single-Point Ramped Imaging with T_1 Enhancement (SPRITE) method, in which the time between excitation and signal detection was maintained as short as possible. The spin echo single-point imaging (SE-SPI) method was used, which is not a direct measure of water content but of the apparent transversal relaxation time distributions ($T_{2,\text{app}}$). The SE-SPI method can serve as a proxy for pore size distributions of saturated porous media (Coates et al., 1999). Longitudinal relaxation time (T_1) measurements were used as complementary relaxation time data.

Apparent Transversal Relaxation Time Distribution Spectra

Spin–spin (T_2) relaxation time measurements are powerful methods to obtain information about the local environment of water molecules confined in a porous material (Jaeger et al., 2009). The T_2 values are mainly influenced by pore size, paramagnetic impurities, characteristic detection parameters (e.g., the echo time), and other variables (Barrie, 2000). The relaxation rate, which can be measured using a CPMG sequence, can be split into rates that represent the contribution of different processes to the transverse signal decay of water in porous materials as

$$\frac{1}{T_2}=\frac{1}{T_{2,\text{bulk}}}+\rho_2\left(\frac{S}{V}\right)+\frac{1}{T_{2,\text{diffusion}}} \qquad [1]$$

where $1/T_{2,\text{bulk}}$ is the relaxation rate of the bulk solution, ρ_2 is the T_2 surface relaxivity parameter, S/V is the ratio of pore surface to fluid volume, and $1/T_{2,\text{diffusion}}$ represents the signal loss rate due to diffusion in magnetic field gradients, which depends on the echo time (t_E) used. The bulk relaxation rate of pure water is usually in the range of 0.333 s^{-1} and is much smaller than the relaxation rates due to other interactions in porous media. Because it is not always possible to eliminate the decay rate due to diffusion in internal (or external) magnetic field gradients, it is convenient to define an apparent transverse relaxation rate (Pomerantz et al., 2008):

$$\frac{1}{T_{2,\text{app}}}=\rho_2\left(\frac{S}{V}\right)+\frac{1}{T_{2,\text{diffusion}}\left(t_E\right)} \qquad [2]$$

The CPMG sequence is a standard method to measure the decay of the transverse magnetization. Typically it uses a radio-frequency (rf) pulse that rotates the magnetization by 90°, followed by a series of 180° pulses generating n spin echoes, each separated by t_E. The decay of the magnetization is described by

$$M(t,r)=M(0,r)\exp\left(\frac{-t}{T_{2,\text{app}}}\right) \qquad [3]$$

where $M(0,r)$ is the initial signal amplitude, and $t = n_E t_E$, where n_E is the number of echoes and t_E is the echo time.

Spin echo single-point imaging T_2 mapping provides spatially resolved measurements of the apparent transverse relaxation time (McIntosh, 2013; Petrov et al., 2011). After a 90° rf pulse, a stepped gradient pulse is applied that varies in strength for each repetition. Thereafter, a series of n 180° pulses creates n_E echoes after $n_E t_E$, similar to a CPMG echo train. The signal intensity at $t = t_{E,0} + (n_E - 1)t_E$ is given by

$$M(t,r)=M(0,r)\exp\left(\frac{-t_{E,0}}{T_{2,\text{app}}}\right)\exp\left[-\left(n_E-1\right)\left(\frac{t_E}{T_{2,\text{app}}}\right)\right] \qquad [4]$$

where $t_{E,0}$ and t_E are the echo times after the first pulse and the subsequent intervals, respectively. If a Fourier transformation is applied to the raw data along the stepped gradient dimension followed by an inverse Laplace transformation along the $n_E t_E$ direction, a $T_{2,\text{app}}$ distribution for each data point in the region of interest can be obtained.

Determination of Soil Moisture Using One-Dimensional Centric Scan SPRITE

A one-dimensional centric scan SPRITE method with centric scanning of k-space was used for moisture monitoring (Bernstein et al., 2004; Mastikhin and Balcom, 2012; Muir and Balcom, 2012). The signal intensity is given by

$$M(t,r)=M(0,r)\exp\left(\frac{-t_p}{T_2^*}\right)\sin\alpha \qquad [5]$$

where α is the flip angle of the excitation pulse, and t_p is the time between the excitation pulse and the data acquisition. The value of T_2^* is given by $1/T_2^* = 1/T_{2,\text{app}} + 1/T_{2,\text{inhomogeneous}}$, where the latter describes the dephasing driven by static inhomogeneities of the magnetic field. With $t_p < T_2^*$, the signal is directly proportional to the moisture content in the sample $M(0,r)$. The characteristic parameters of all MR methods described above are summarized in Table 1.

Table 1. Acquisition parameters of the Carr–Purcell–Meiboom–Gill (CPMG), spin echo single-point imaging (SE-SPI), and single-point ramped imaging with longitudinal relaxation time enhancement (SPRITE) magnetic resonance methods.

	Short sample			Long sample		
Acquisition parameter	CPMG	SE-SPI	SPRITE	CPMG	SE-SPI	SPRITE
Flip angle (α), degrees	90	90	2.6	90	90	3.3
Repetition time (t_R), ms	1000	600	200	1000	500	600
Encoding time (t_p), ms	–	–	0.125	–	–	0.125
First echo time ($t_{E,0}$), ms	0.25	0.72	–	0.25	0.72	–
Subsequent echo time (t_E), ms	0.25	0.7	–	0.25	0.7	–
Number of echoes (n_E)	1024	512	–	1024	512	–
Number of scans	128	128	128	128	4	500
Measurement time, min	3	30	0.7	3	4	3

Longitudinal Relaxation Time by Means of Inversion Recovery

Inversion recovery is the most commonly used method to measure the longitudinal relaxation time constant T_1. In contrast to T_2, longitudinal relaxation is not affected by diffusion in internal gradients. This method uses an initial 180° pulse. The time evolution of magnetization is thus described by

$$M(t,r)=M(0,r)\left[1-2\exp-\left(\frac{t}{T}\right)\right] \qquad [6]$$

where T_1 is the longitudinal relaxation time constant (Abragam, 1961). If a Fourier transformation is applied to the raw data followed by an inverse Laplace transformation along the inversion time direction t, a T_1 distribution can be obtained.

Modeling Moisture Development

All variables used for moisture modeling are given in Table 2.

The Richards Equation

To describe vertical water movement in the vadose zone, the one-dimensional Richards equation (Richards, 1931) is traditionally used:

$$\frac{\partial\theta}{\partial t}=\frac{\partial}{\partial z}\left[K(h)\left(\frac{\partial h}{\partial z}+1\right)\right]-S(h) \qquad [7]$$

where θ is the volumetric water content (moisture), h is the pressure head, K is the hydraulic conductivity, t is the time, S is a sink term, and z is the vertical coordinate. In the Richards equation, only liquid water flow in the porous medium is considered, where this flow is assumed to be independent from temperature gradients in the porous medium. The hydraulic conductivity function $K(h)$ and the moisture retention characteristic $\theta(h)$ are given by the Mualem–van Genuchten parameterization with

$$(h)=\left[1+(\alpha|h|)^{n}\right]^{1-1/n} \qquad [8]$$

where α is the desaturation coefficient (representing the desaturation rate with increasing matric suction) (Ng and Menzies, 2007), and n describes the soil pore size distribution of the soil. The effective water saturation Θ is given by

$$\Theta(h)=\frac{\theta(h)-\theta_r}{\theta_s-\theta_r} \qquad [9]$$

where θ_s and θ_r are the initial and residual water content, respectively.

The values of θ_s, θ_r, α, and n are determined from a set of measurement points of soil moisture and the corresponding pressure head by minimizing the deviation between $\theta(h)$ from Eq. [8] and the measurements. Frequently, the Mualem–van Genuchten (Mualem, 1976; van Genuchten, 1980) approach is used to determine the unsaturated hydraulic conductivity $K_{Lh}(h)$:

$$K_{Lh}(h)=K_s\frac{\left\{1-(\alpha h)^{n-1}\left[1+(\alpha h)^{n}\right]^{1-1/n}\right\}^{2}}{\left[1+(\alpha h)^{n}\right]^{[(1-1/n)/2]l}} \qquad [10]$$

where K_s is the saturated hydraulic conductivity, and l is a tortuosity factor. To solve the Richards equation, initial and boundary conditions need to be specified. For our simulations, for the top surface of the soil columns, a flux boundary condition was defined during S1 evaporation (i.e., the flux is equal to the measured evaporation flux), and a constant pressure head (Dirichlet) boundary was defined during S2 (i.e., $h_{surface} = -15{,}000$ cm). For the bottom boundary, a no-flow condition was defined.

Coupled Water, Vapor, and Heat Flow Model

Liquid Water and Vapor Flow. For the purpose of this work, the simultaneous movement of water, vapor, and heat was assumed (Bittelli et al., 2008; Saito et al., 2006; Šimůnek et al., (2008), where the liquid water and vapor transport is governed by

Table 2. Variables used for the Richards approach and for the coupled model.

Parameter		Dimension	Value
α	desaturation coefficient	$[\mathrm{L}^{-1}]$	
β_0	water surface tension at 25°C	$[\mathrm{M\,T}^{-1}]$	$= 72\ \mathrm{g\,s}^{-2}$
β	surface tension of soil water	$[\mathrm{M\,T}^{-1}]$	$= 75.6 - 0.1425T - 2.38 \times 10^{-4}\,T^2\ \mathrm{g\,s}^{-2}$
η	enhancement factor		
λ	apparent soil thermal conductivity	$[\mathrm{M\,L\,T}^{-3}\,\mathrm{K}^{-1}]$	
θ	volumetric water content	$[\mathrm{L}^3\,\mathrm{L}^{-3}]$	
θ_s	saturated volumetric water content	$[\mathrm{L}^3\,\mathrm{L}^{-3}]$	
θ_r	residual volumetric water content	$[\mathrm{L}^3\,\mathrm{L}^{-3}]$	
ρ_{vs}	saturated vapor density	$[\mathrm{M\,L}^{-3}]$	
ρ_w	density of liquid water	$[\mathrm{M\,L}^{-3}]$	
Θ	effective water saturation		
d	empirical factor	(K)	$= 2.501 \times 10^6\ \mathrm{K}$
g	gravitational acceleration	$[\mathrm{L\,T}^{-2}]$	$= 9.81\ \mathrm{m\,s}^{-2}$
h	pressure head	[L]	
k	empirical factor		$= 2369.2$
l	pore-connectivity parameter		
n	pore size distribution		
q_h	soil heat flux density	$[\mathrm{M\,T}^{-3}]$	
q_v	flux density of water vapor	$[\mathrm{L\,T}^{-1}]$	
q_w	flux density of liquid water	$[\mathrm{L\,T}^{-1}]$	
t	time	[T]	
z	vertical coordinate	[L]	
C_v	volumetric heat capacity of liquid water	$[\mathrm{M\,L}^{-1}\,\mathrm{T}^{-2}\,\mathrm{K}^{-1}]$	$4.18\ \mathrm{MJ\,m}^{-1}\,\mathrm{K}^{-1}$
C_w	volumetric heat capacity of water vapor	$[\mathrm{M\,L}^{-1}\,\mathrm{T}^{-2}\,\mathrm{K}^{-1}]$	$1.8\ \mathrm{MJ\,m}^{-1}\,\mathrm{K}^{-1}$
C_p	volumetric heat capacity of the moist soil	$[\mathrm{M\,L}^{-1}\,\mathrm{T}^{-2}\,\mathrm{K}^{-1}]$	
D_v	soil vapor diffusivity	$[\mathrm{L}^2\,\mathrm{T}^{-1}]$	
G_{wT}	gain factor		
H_r	fractional relative humidity		
K	hydraulic conductivity	$[\mathrm{L\,T}^{-1}]$	
K_{Lh}	unsaturated hydraulic conductivity	$[\mathrm{L\,T}^{-1}]$	
K_{LT}	liquid phase thermal hydraulic conductivity	$[\mathrm{L}^2\,\mathrm{K}^{-1}\,\mathrm{T}^{-1}]$	
K_s	saturated hydraulic conductivity	$[\mathrm{L\,T}^{-1}]$	
K_{vh}	isothermal vapor hydraulic conductivity	$[\mathrm{L\,T}^{-1}]$	
K_{vT}	thermal vapor hydraulic conductivity	$[\mathrm{L}^2\,\mathrm{K}^{-1}\,\mathrm{T}^{-1}]$	
L_0	volumetric latent heat of vaporization	$[\mathrm{L}^2\,\mathrm{T}^{-2}\,\mathrm{L}^{-3}]$	
M_w	molecular weight of water	$[\mathrm{M\,N}^{-1}]$	$= 0.018015\ \mathrm{kg\,mol}^{-1}$
Q	heat sink or source	$[\mathrm{M\,L}^{-1}\,\mathrm{T}^{-2}\,\mathrm{K}^{-1}]$	
R	universal gas constant	$[\mathrm{M\,L}^2\,\mathrm{T}^{-2}\,\mathrm{K}^{-1}\,\mathrm{M}^{-1}]$	$= 8.314\ \mathrm{J\,mol}^{-1}\,\mathrm{K}^{-1}$
S	sink term	$[\mathrm{T}^{-1}]$	
S_h	soil heat storage	$[\mathrm{L}^2\,\mathrm{T}^{-2}\,\mathrm{L}^{-3}]$	
T	absolute temperature	(K)	

$$\frac{\partial \theta}{\partial t} = \frac{\partial}{\partial z}\left(K_{\mathrm{Lh}}\frac{\partial h}{\partial z} + K_{\mathrm{Lh}} + K_{\mathrm{LT}}\frac{\partial T}{\partial z} + K_{\mathrm{vh}}\frac{\partial h}{\partial z} + K_{\mathrm{vT}}\frac{\partial T}{\partial z}\right) - S \qquad [11]$$

where S is a sink term that usually accounts for root water uptake. Because only bare soils are considered, S is neglected. The isothermal unsaturated hydraulic conductivity $K_{\mathrm{Lh}}(h)$ is calculated by using the Mualem–van Genuchten approach according to Eq. [10]. The thermal hydraulic conductivity K_{LT} is defined as

$$K_{\mathrm{LT}} = K_{\mathrm{Lh}}\left(hG_{\mathrm{wT}}\frac{1}{\beta_0}\frac{\mathrm{d}\beta}{\mathrm{d}T}\right) \qquad [12]$$

where G_{wT} is a gain factor that describes the temperature dependence of the soil water retention curve (Nimmo and Miller, 1986), β_0 is the surface tension of water at 25°C, β is the surface tension at a certain temperature, K_{vh} is the isothermal vapor hydraulic conductivity, and K_{vT} is the thermal vapor hydraulic conductivity, given by an empirical relation as (Andreas, 2005; Bittelli et al., 2008):

$$K_{\mathrm{vh}} = \frac{D_{\mathrm{v}}}{\rho_{\mathrm{w}}}\rho_{\mathrm{vs}}\frac{M_{\mathrm{w}}g}{RT}H_{\mathrm{r}} \qquad [13]$$

$$K_{\mathrm{vT}} = \frac{D_{\mathrm{v}}}{\rho_{\mathrm{w}}}\eta H_{\mathrm{r}}\frac{\mathrm{d}\rho_{\mathrm{vs}}}{\mathrm{d}T} \qquad [14]$$

where D_{v} is the vapor diffusivity in soil; ρ_{vs} and ρ_{w} are the saturated vapor density and the density of liquid water, respectively; M_{w} is the molecular weight of water; g is the acceleration due to gravity; R is the gas constant; η is an enhancement factor (Cass et al., 1984) accounting for the increased thermal vapor fluxes caused by increasing temperature gradients in the air phase; and H_{r} is the relative humidity (Philip and De Vries, 1957):

$$H_{\mathrm{r}} = \exp\left[\frac{M_{\mathrm{w}}g(h/100)}{RT}\right] \qquad [15]$$

Heat Transport. The movement of energy is given by the energy conservation equation:

$$\frac{\partial S_{\mathrm{h}}}{\partial t} = -\frac{\partial q_{\mathrm{h}}}{\partial z} - Q \qquad [16]$$

where Q can be a heat sink or source, and S_{h} is the soil heat storage, given by

$$S_{\mathrm{h}} = C_{\mathrm{p}}T + L_0\theta \qquad [17]$$

where C_p is the volumetric heat capacity of the moist soil, and L_0 is the latent heat of vaporization, given as

$$L_0 = (d - kT)\rho_w \quad [18]$$

where d and k are empirical factors.

The total soil heat flux density is governed by

$$q_h = -\lambda \frac{\partial T}{\partial z} + C_w (T - T_r) q_w + C_v (T - T_r) q_v + L_0 q_v \quad [19]$$

where λ is the thermal conductivity (Chung and Horton, 1987); C_w and C_v are the volumetric heat capacities of liquid water and water vapor, respectively; T_r is an arbitrary reference temperature; and q_v and q_w are flux densities of water vapor and liquid water, respectively.

As boundary conditions, we defined air temperature (25°C) and relative air humidity (65%). The incoming long-wave radiation was calculated from the emissivity of the soil surface (0.9) and the emitted radiation of a black body with a temperature of 25°C, representing the radiation of the walls inside the chamber. The outgoing long-wave radiation was calculated from emissivity and the simulated temperature of the soil surface. The wind speed, which is used to calculate the aerodynamic resistance for latent and sensible heat transfer between the soil surface and the atmosphere, was fitted such that the evaporation rate of a wet surface was equal to the average evaporation rate during S1 for each sample. The simulations were computed using the HYDRUS (PC-Progress) code implemented in a MATLAB (R2011a, The MathWorks) environment.

Materials and Methods

Soil Samples and Hydraulic Properties

Two cylindrical Perspex columns (60 mm in length and 38 mm in diameter) were packed with (i) a silt loam and (ii) a sandy loam. A third cylindrical glass column (500 mm in length and 33 mm in diameter) was packed with the identical sandy loam. All soil samples originated from the test sites of the Potato Research Center in Fredericton, NB, Canada (45°55′4.2″ N, 66°36′29.4″ W) and were sieved to <2 mm and oven dried at 105°C. Each column was initially saturated from the bottom, which was sealed after saturation. Thus, evaporation could only occur at the column surface. All three samples were insulated (Armaflex, Armacell GmbH) to eliminate heat exchange via the column wall. The samples were stored in a climate chamber (Caron 6010) under a constant temperature of 25°C and a relative humidity of 65% between the MR measurements. The soil hydraulic properties were determined by means of the HYPROP-Laboratory evaporation method (UMS GmbH) (Peters and Durner, 2008; Schindler et al., 2010a), which consists of monitoring the decrease in water content and matric potential in a soil sample driven by evaporation. The obtained soil hydraulic property values were further cross-checked using the ROSETTA database (Schaap et al., 2001). The water retention function and characteristic parameters of the different soils and samples are shown in Fig. 1 and summarized in Table 3.

Magnetic Resonance Setup

A vertical bore MARAN DRX-HF imaging system (Oxford Instruments), equipped with 1-kW Techron gradient amplifiers (Type 7782, AETechron), water-cooled gradient coils, and a custom-built rf resonator with a resonance frequency of 8.5 MHz and an inner diameter of 45 mm, was used to monitor the short samples. The specimens were placed vertically inside the probe by means of a laboratory jack to reproduce an identical position for each measurement. Measurements of the long sandy loam column were performed using a vertical-bore MARAN DRX spectrometer (Oxford Instruments) equipped with a 25-W amplifier and an rf probe with an inner diameter of 51 mm operating at a resonance frequency of 2.2 MHz. The vertical measurement spot of the probe was restricted to 50 mm, and the long sample was therefore measured in 10 steps to acquire the overall length of 500 mm by using a laboratory jack that was raised 50 mm after each measurement.

Moisture Profiles and Relaxation Time Distributions

To achieve moisture profiles for each column as a function of time, the raw MR SPRITE data point intensity (Eq. [5]) of the 60-mm sandy loam and silt loam columns were processed as follows. The local intensity of the one-dimensional profile was calibrated using an external reference placed above the sample consisting of 60% (w/w) D_2O and 40% (w/w) H_2O. A resolution of 2 mm per data point was set by a field of view of 128 mm for the 64 points in

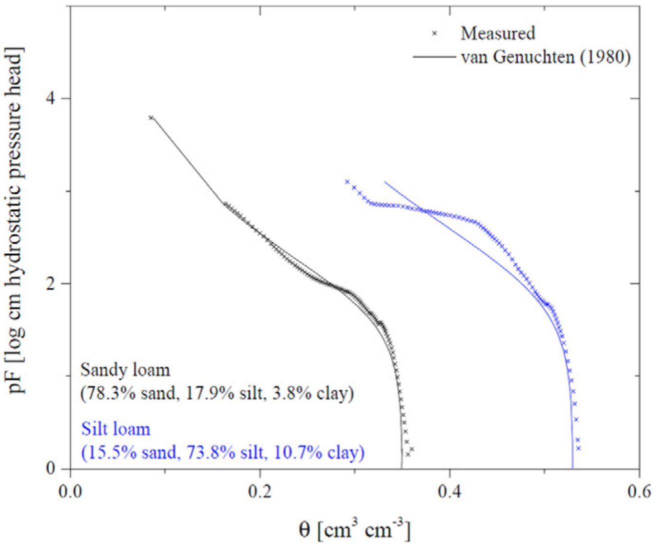

Fig. 1. Measured (crosses) water retention curves of the sandy loam (black) and the silt loam (blue) using the HYPROP evaporation method and fitted (line) based on van Genuchten (1980).

Table 3. Soil composition, van Genuchten–Mualem parameters, bulk density (ρ_b), and porosity (ε) for the silt loam and sandy loam.

Soil	ρ_b		ε									
	Short sample	Long sample	Short sample	Long sample	n	α	θ_r	K_s	l	Sand	Silt	Clay
	—— g cm^{-1} ——					cm^{-1}		cm d^{-1}		—— % ——		
Sandy loam	1.6	1.6	0.35	0.39	1.3	0.05	0.03	100	0.5	78.3	17.9	3.8
Silt loam	1.2	–	0.5	–	1.2	0.03	0.09	50	0.5	15.5	73.8	10.7

the vertical direction. The SE-SPI data were fitted, and the final distributions were generated using a home-built data processing routine used in the MATLAB environment to achieve spatially resolved $T_{2,\mathrm{app}}$ distributions. The CPMG measurements were processed using an inverse Laplace algorithm as implemented in the WinDXP (Resonance Instruments Ltd) package and the Winfit (Bruker) software to obtain bulk $T_{2,\mathrm{app}}$ distributions with 128 data points. The T_1 data were processed in an identical fashion as the $T_{2,\mathrm{app}}$ data using 33 data points. Because the size of the resonator did not allow measuring the 500-mm sandy loam column as a whole, the column was divided into 10 compartments, and the data of each compartment were processed as described above.

Effective Saturation and Relative Evaporation Rate

The effective saturation (Θ) and the relative evaporation rate (e/e_0) were determined gravimetrically every 24 h for the short silt and sandy loam columns and for the long sandy loam column. The value of Θ was calculated according to Eq. [6] with $\theta_s = 0.9\varepsilon$ (Rogowski, 1971) and $\varepsilon = 1 - \rho_b/\rho_{\mathrm{grain}}$, where ρ_b is the bulk density, and ρ_{grain} is the particle density, which is assumed to be 2.65 g cm^{-3} (Cameron and Buchan, 2005). Because the pan evaporation rate (e_0) was found to be constant at 3.9 mm d^{-1}, the relative evaporation (e/e_0) was calculated from the daily evaporation of each sample.

Evaluation of the Fitting Model Performances

The measured and simulated evaporation rates (using both the Richards equation and the coupled model) were compared with each other for the 60-mm silt and sandy loam columns and the 500-mm sandy loam column. The performance of both models was evaluated using r^2, RMSE, and the coefficient of efficiency (NSE) according to Nash and Sutcliffe (1970) with logarithmic values:

$$r^2 = \frac{\sum (P_i - \bar{O})^2}{\sum (O_i - \bar{O})^2} \qquad [20]$$

$$\mathrm{RMSE} = \sqrt{\frac{\sum_i^n (O_i - P_i)^2}{\mathrm{n}}} \qquad [21]$$

$$\mathrm{NSE} = 1 - \frac{\sum_{i=1}^n \left(\ln O_i - \ln P_i\right)^2}{\sum_{i=1}^n (\ln O_i - \bar{O})^2} \qquad [22]$$

where O and P are the measured and predicted data at the ith time or position, respectively, and $\bar{O}$ is the mean value of the measured data. Using the logarithmic values of O and P for calculating the NSE reduces the oversensitivity to extreme values caused by the mean square error (Krause et al., 2005; Legates and McCabe, 1999), where the range of NSE lies between 1 and $-\infty$. Higher values of NSE indicate a better agreement; for example, NSE = 1 means a perfect fit, NSE = 0 indicates that $\bar{O}$ (the observed mean) and the model are equally good, and NSE < 0 (the mean square error exceeds the variance) indicates that $\bar{O}$ is a better predictor than the model.

Results and Discussion

Evolution of the Relative Evaporation Rate and the Effective Saturation

The effective saturation and the measured and modeled relative evaporation rates are shown as functions of time in Fig. 2a and 3a for the 60-mm sandy loam and silt loam columns, respectively, and in Fig. 4 for the 500-mm sandy loam column. The relative evaporation rate e/e_0 of all columns dropped below 1 right after the columns were exposed to evaporation in the climate chamber. During S1, e/e_0 remained constant for all columns and coincided with a linear decrease in the effective saturation. At the transition between S1 and S2, e/e_0 of all columns decreased considerably due to the development of a dry surface layer. Simultaneously, the effective saturation declined during the transition as compared with S1 as evaporation became soil limited; that is, soil properties such as the pore size distribution (n) and the unsaturated hydraulic conductivity $K(h)$ control the moisture depletion of the soil to a large extent and thus control the depth of the dry surface layer. Therefore, the good correspondence between the simulated and observed shift in evaporation stage and between the simulated and observed evaporation during S2 demonstrates the predictive power of the simulation model to represent evaporation fluxes from the porous medium. Based on the simulated evaporation rates, the model was used in the subsequent step to simulate the development of vertical moisture profiles for all columns.

Moisture Profiles Monitored by Magnetic Resonance

Moisture data of the 60- and 500-mm sandy loam columns (Fig. 2b–2d and 4b–4d) and of the 60-mm silt loam column (Fig.

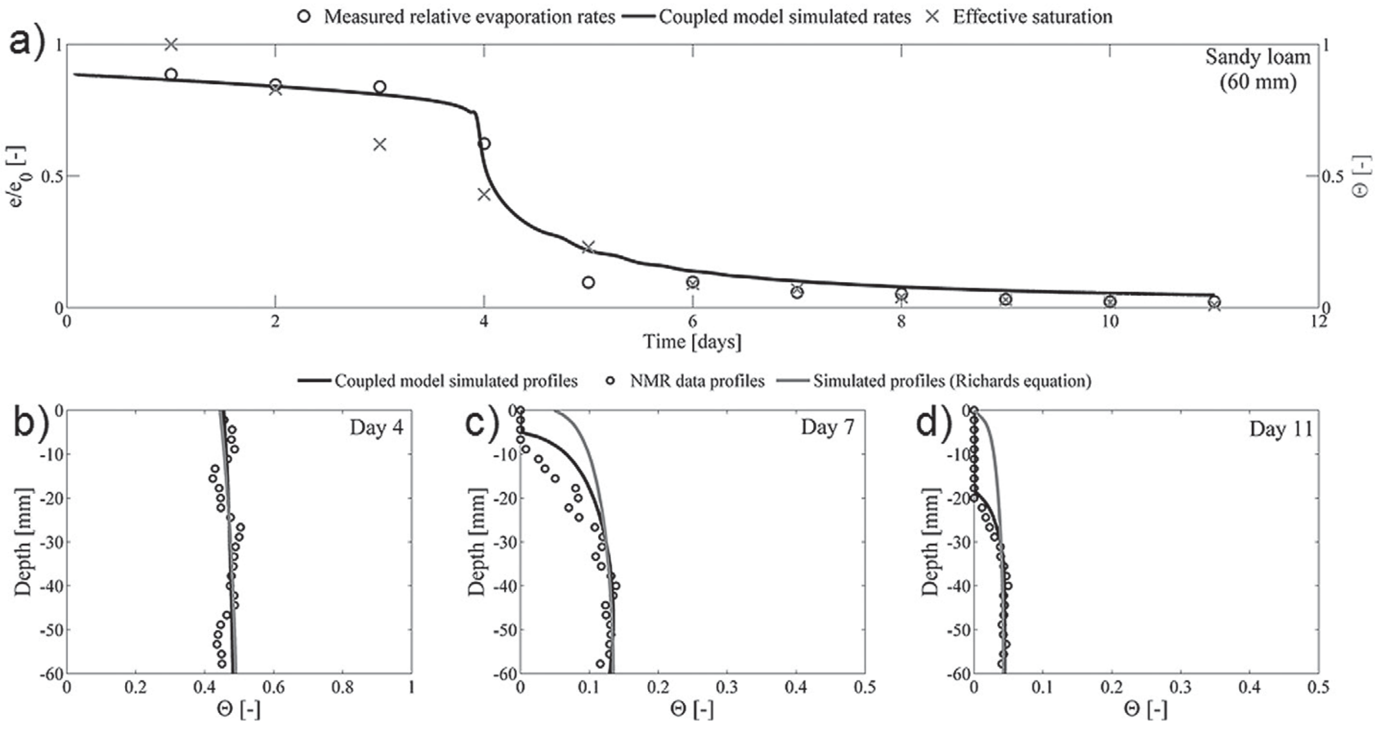

Fig. 2. Sandy loam column (60 mm): (a) measured relative evaporation rates e/e_0 (circles), measured effective saturation Θ (crosses), and the coupled model-simulated e/e_0 (black line); (b–d) corresponding measured effective saturation Θ (circles) as a function of depth monitored by magnetic resonance, the coupled model-simulated profiles (black lines), and the profiles of the one-dimensional Richards equation (gray lines) after (b) 4, (c) 7, and (d) 11 d of drying.

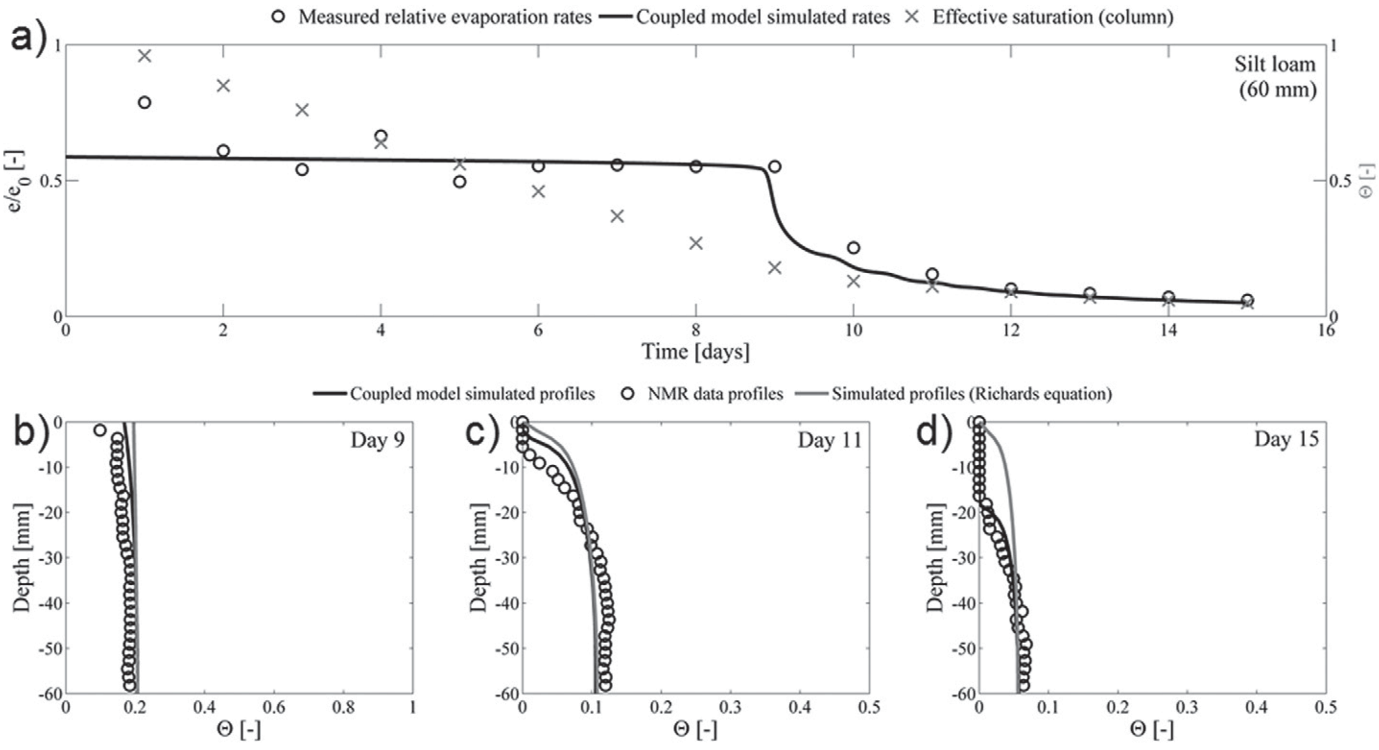

Fig. 3. Silt loam column (60 mm): (a) measured relative evaporation rates e/e_0 (circles), measured effective saturation Θ (crosses), and the coupled model-simulated e/e_0 (black line); (b–d) corresponding measured Θ (circles) as a function of depth monitored by magnetic resonance, the coupled model-simulated profiles (black lines), and the profiles of the one-dimensional Richards equation (gray lines) after (b) 9, (c) 11, and (d) 15 d of drying.

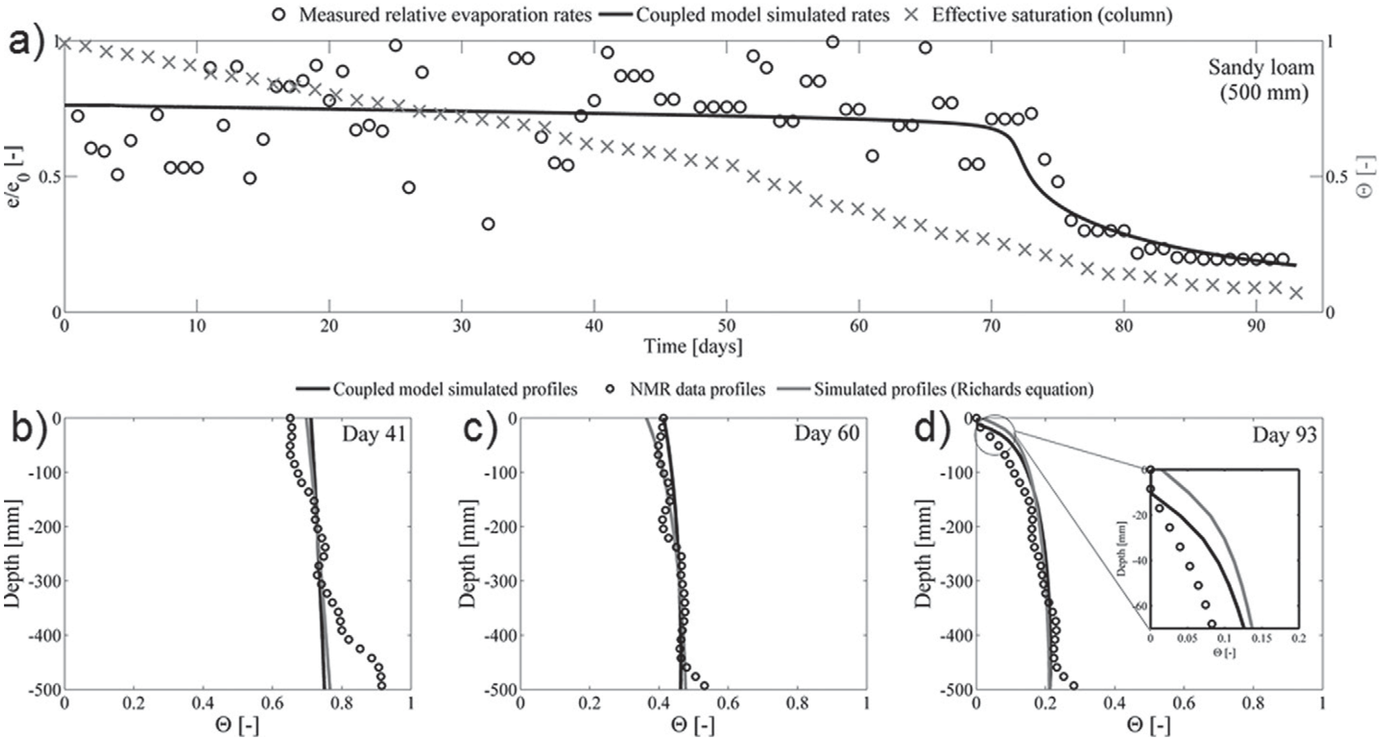

Fig. 4. Sandy loam column (500 mm): measured relative evaporation rates e/e_0 (circles), measured effective saturation Θ (crosses), and the coupled model-simulated e/e_0 (black line); (b–d) corresponding measured and spline-interpolated Θ (circles) as a function of depth monitored by magnetic resonance, the coupled model-simulated profiles (black lines), and the profiles of the one-dimensional Richards equation (gray lines) after (b) 41, (c) 60, and (d) 93 d of drying.

3b–3d) were computed as effective saturation vs. depth according to Eq. [8]. For each column, three representative plots at different stages of desaturation are displayed: right before the onset of S2 (Fig. 3b), 2 d after the transition from S1 to S2 (Fig. 3c), and at the final state of the experiment (6 d after the onset of S2) (Fig. 3d). During S1, the moisture is homogeneously distributed without any significant moisture gradient for the 60-mm silt loam and sandy loam columns (Fig. 2b and 3b). For the 500-mm sandy loam profile, the moisture also shows a homogenous distribution with a slight gradient of $\Delta\Theta/\Delta z = 9 \times 10^{-4}$ mm^{-1} at Day 41 from the bottom to the top, which disappeared after 60 d of drying (Fig. 4b and 4c). During the first stage of drying, the moisture profiles of all columns were in good agreement with the profiles simulated by the coupled model and the one-dimensional Richards approach. As the soil dried out, a gradient in moisture developed from the bottom up to the evaporation front that moved inside the soil profile, marking the onset of S2. This evaporation front is therefore referred to as the *secondary evaporation front* (Merz et al., 2015b). Two days after the onset of S2, the effective saturation of both 60-mm columns decreased from $\Theta = 0.1$ at the bottom of the columns to $\Theta = 0$ at the secondary evaporation located at a depth of 10 mm.

The coupled model predicts the measured profiles satisfactorily, whereas the one-dimensional Richards model did not show any dry surface layer because it does not account for vapor and heat transport and is therefore unable to predict accurately under S2 conditions (Fig. 2c, 2d, 3c, and 3d). Therefore, the profiles obtained with the one-dimensional Richards equation overestimate the moisture content particularly in the upper part of the 60-mm columns. At the final experimental stage, the secondary evaporation front was located at a depth of 20 mm for the 60-mm sandy and silt loam columns (Fig. 2d and 3d) and around 10 mm for the 500-mm sandy loam column (Fig. 4d). The one-dimensional Richards approach could not reproduce the dry surface layer, yielding an overall deviation in absolute water content above the drying front of $\theta = 0.18$ cm^3 cm^{-3} for the 60-mm silt loam and $\theta = 0.12$ cm^3 cm^{-3} for the 60-mm sandy loam column, which is equal to an error of approximately 50% between the Richards approach and the MR data compared with the initial saturation. For the 500-mm sandy loam column, the overall deviation in water content above the dry layer after 93 d was approximately 16% and corresponded to $\theta = 0.05$ cm^3 cm^{-3}. This trend was reflected by an increasing RMSE and a decreasing NSE (Table 4). Experimental results and predictions by the coupled model agreed increasingly with time for all columns, resulting in a decreasing RMSE and an increasing NSE. For the one-dimensional Richards profiles, an opposed trend with increasing RMSE and a decrease in NSE over time is found because this approach relies solely on liquid water flow. In summary, the overall trend of the Richards approach leads to larger deviations from experimental observations with progressing desaturation of the soil. The strong bias in moisture content for

Table 4. Calculated performance criteria of the correspondence between the measured relative evaporation rates (e/e_0) and the simulated rates using a coupled water, heat, and vapor flow model; the effective saturation (Θ) profiles determined by means of magnetic resonance and the coupled model-simulated vertical Θ profiles; and the Θ profiles determined by means of magnetic resonance and the vertical one-dimensional Richards equation Θ profiles.

		Silt loam (60 mm)				Sandy loam (60 mm)				Sandy loam (500 mm)			
Model	Parameter	e/e_0	9 d	11 d	15 d	e/e_0	4 d	7 d	11 d	e/e_0	41 d	60 d	93 d
Coupled model	NSE†	0.96	−1.29	0.51	0.81	0.90	−0.12	0.34	0.90	0.81	0.21	0.53	0.92
	R^2	0.95	0.94	0.94	0.96	0.99	0.95	0.94	0.98	0.78	0.94	0.82	0.94
	RMSE	0.076	0.03	0.02	0.007	0.048	0.08	0.02	0.003	0.17	0.07	0.02	0.03
Richards equation	NSE		−2.86	−115.0	−264		−0.4	−911	−322		0.38	0.65	0.29
	R^2		0.92	0.84	0.84		0.92	0.84	0.85		0.94	0.84	0.94
	RMSE		0.034	0.083	0.12		0.026	0.035	0.04		0.07	0.02	0.06

† Nash–Sutcliffe coefficient of efficiency.

the topmost soil layer clearly demonstrates that accurate moisture profiles are predictable only if vapor and heat flow are considered in addition to liquid water flow, as demonstrated by Fetzer et al. (2017) and Vanderborght et al. (2017).

Relaxation Time Spectra during Drying

Complementary to the moisture profiles, T_1 and $T_{2,\mathrm{app}}$ relaxation times can serve as proxy for the pore size distribution under saturated conditions and enable the determination of the secondary evaporation front. In contrast to $T_{2,\mathrm{app}}$, T_1 is insensitive to diffusion in internal gradients but averages across small and larger pores in the case of fast exchange (Kleinberg and Horsfield, 1993; Stingaciu et al., 2010). Nevertheless, the information gained from both relaxation time spectra is complementary. The bulk T_1 and $T_{2,\mathrm{app}}$ relaxation time spectra obtained by means of an inverse Laplace transform using Eq. [6] and [3] as kernels are given in Fig. 5 and 6 for the 60-mm sandy and silt loam columns and for the 500-mm sandy loam column, respectively. Under saturated conditions, the bulk T_1 of the small sandy loam column showed a bimodal distribution with a slow mode around 70 ms and a fast mode around 6 ms, whereas a slow mode and a fast mode of around 50 and 3 ms, respectively, were found for the large sandy loam column. The shorter values of mean T_1 for the 500-mm column were caused by the different Larmor frequencies of the instruments; it is known that T_1 relaxation of water in soil materials shows a moderate frequency dispersion effect (Haber-Pohlmeier et al., 2014). The bimodality of the T_1 distribution could not be resolved for the 60-mm silt loam. During desaturation, the

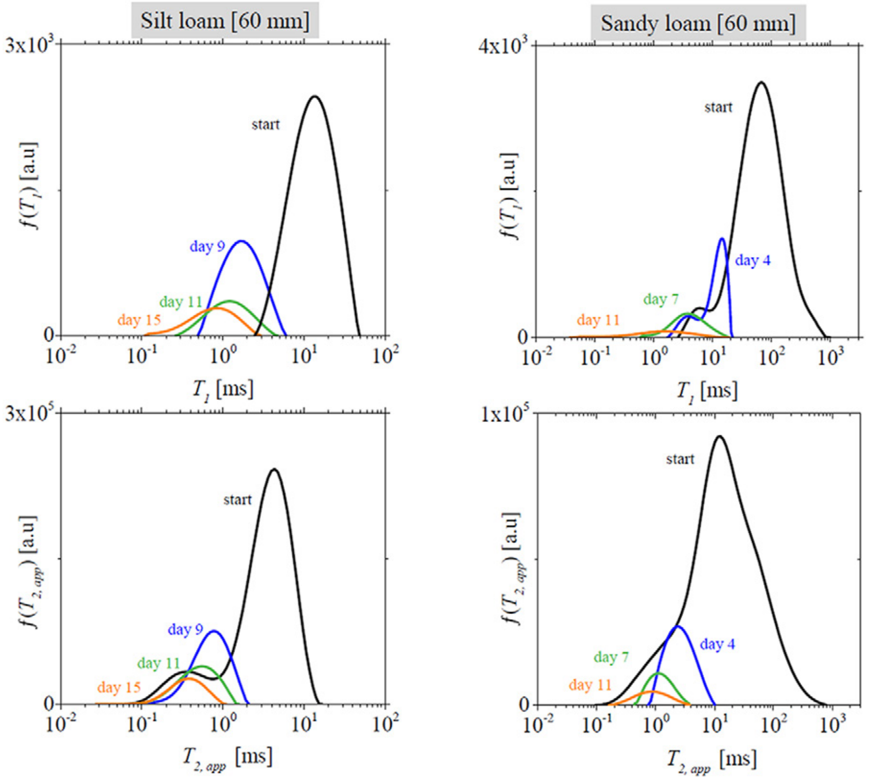

Fig. 5. The (a) longitudinal relaxation time (T_1) and (b) apparent transversal relaxation time distribution ($T_{2,\mathrm{app}}$) spectra (measured at 8.5 MHz) of the 60-mm silt loam and sandy loam columns with time. The $T_{2,\mathrm{app}}$ and T_1 values were determined using a bulk Carr–Purcell–Meiboom–Gill and inversion recovery method, respectively.

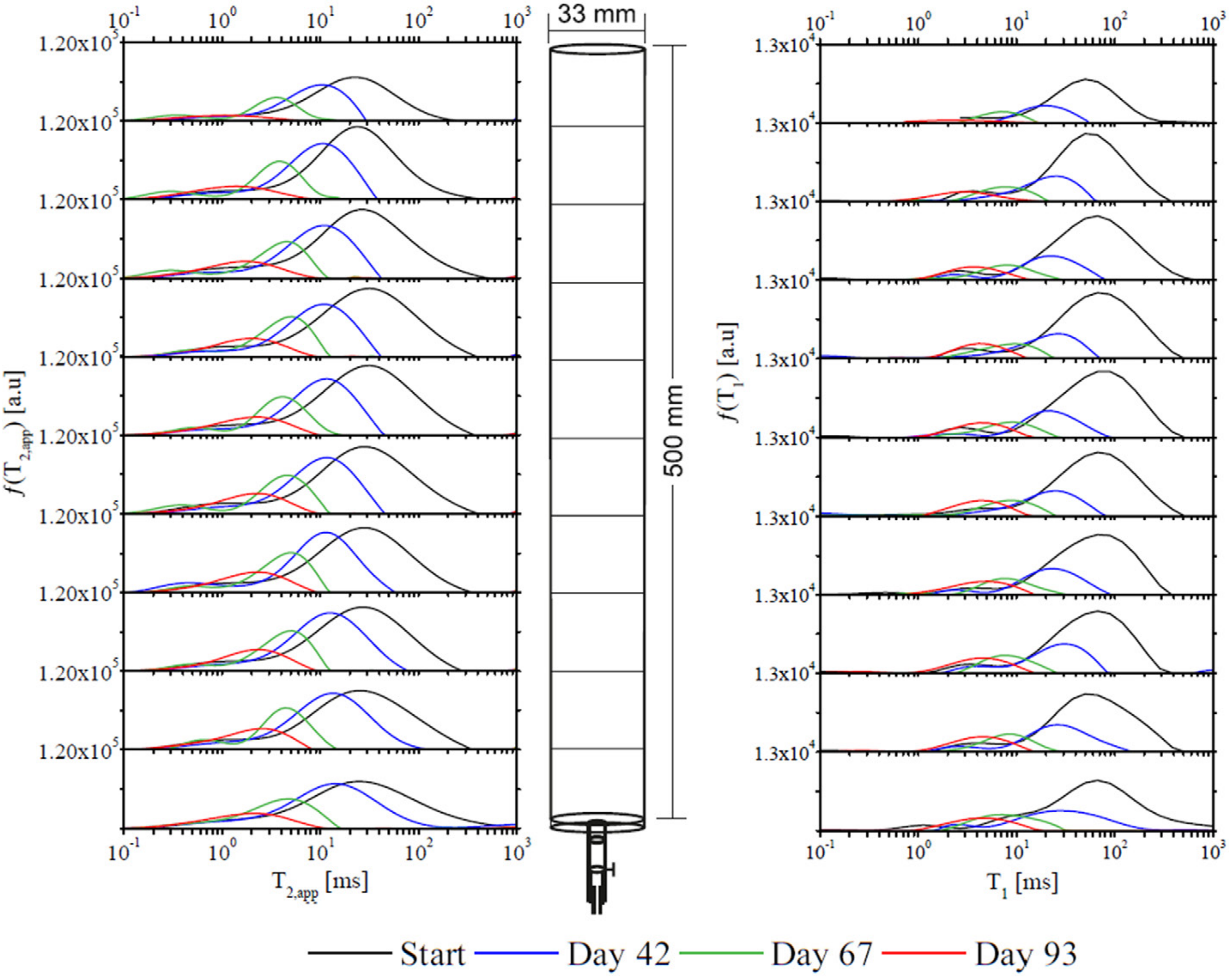

Fig. 6. The apparent transversal relaxation time distribution ($T_{2,app}$) (left) and longitudinal relaxation time (T_1) (right) spectra (measured at 2.2 MHz) for the 500-mm sandy loam column as a function of drying time. The $T_{2,app}$ and T_1 values were determined using a bulk Carr–Purcell–Meiboom–Gill and inversion recovery method, respectively.

amplitudes of the relaxation curves (i.e., the areas of the T_1 distribution curves which are proportional to the moisture content) decreased for all columns and the bimodality of the sandy loam profiles vanished. The mean T_1 relaxation shifted to faster values because progressing moisture depletion confined water primarily in small pores and films.

Because relaxation effects are primarily caused by the environment of the water (i.e., pore surface), the distribution function of relaxation times under saturated conditions can serve as a proxy for the pore size distribution of a saturated porous medium (Stingaciu et al., 2010), provided that the fast diffusion limit is assumed and the average surface relaxivity ρ is known (Duschl et al., 2015).

A recalculation of the MR relaxation time distribution functions to differential pore size distribution functions is possible by scaling the average pore size obtained from water retention curves to the average relaxation time. However, because this is just a rescaling of data, we proceed to discuss the behavior in the time domain. Under saturated conditions, where all accessible pores are assumed to be water filled, the bulk $T_{2,app}$ distributions were bimodal for the 60-mm silt loam column (Fig. 5) with a fast and a slow mode around 4 and 0.3 ms, respectively. The fast $T_{2,app}$ mode of the 60-mm sandy loam column (Fig. 5) was covered under the broad shoulder in the relaxation time spectrum. The profile for the 500-mm column (Fig. 6) shows a bimodal $T_{2,app}$ distribution, with a large shoulder at fast relaxation time enveloping the fast mode.

The integral $T_{2,app}$ measurements (Eq. [3]), which are proportional to the soil moisture content, were in good agreement with the spatially resolved $T_{2,app}$ distributions (Fig. 7 and 8). The 60-mm sandy loam column showed a bimodal $T_{2,app}$ (Fig. 7) distribution,

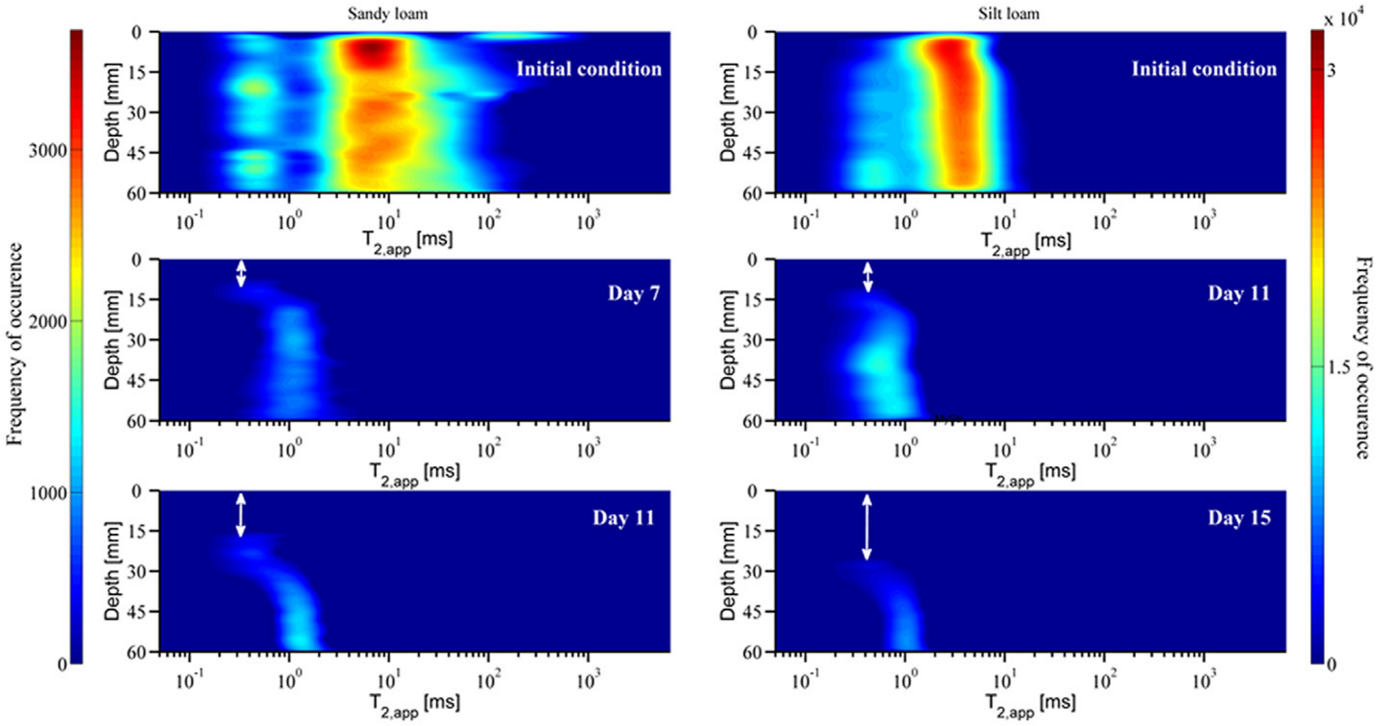

Fig. 7. The apparent transversal relaxation time distribution ($T_{2,\mathrm{app}}$) spectra as a function of drying time of the 60-mm sandy loam (left) and silt loam (right) columns monitored at 8.5 MHz by means of spin echo single-point imaging with a resolution of 2 mm per data point.

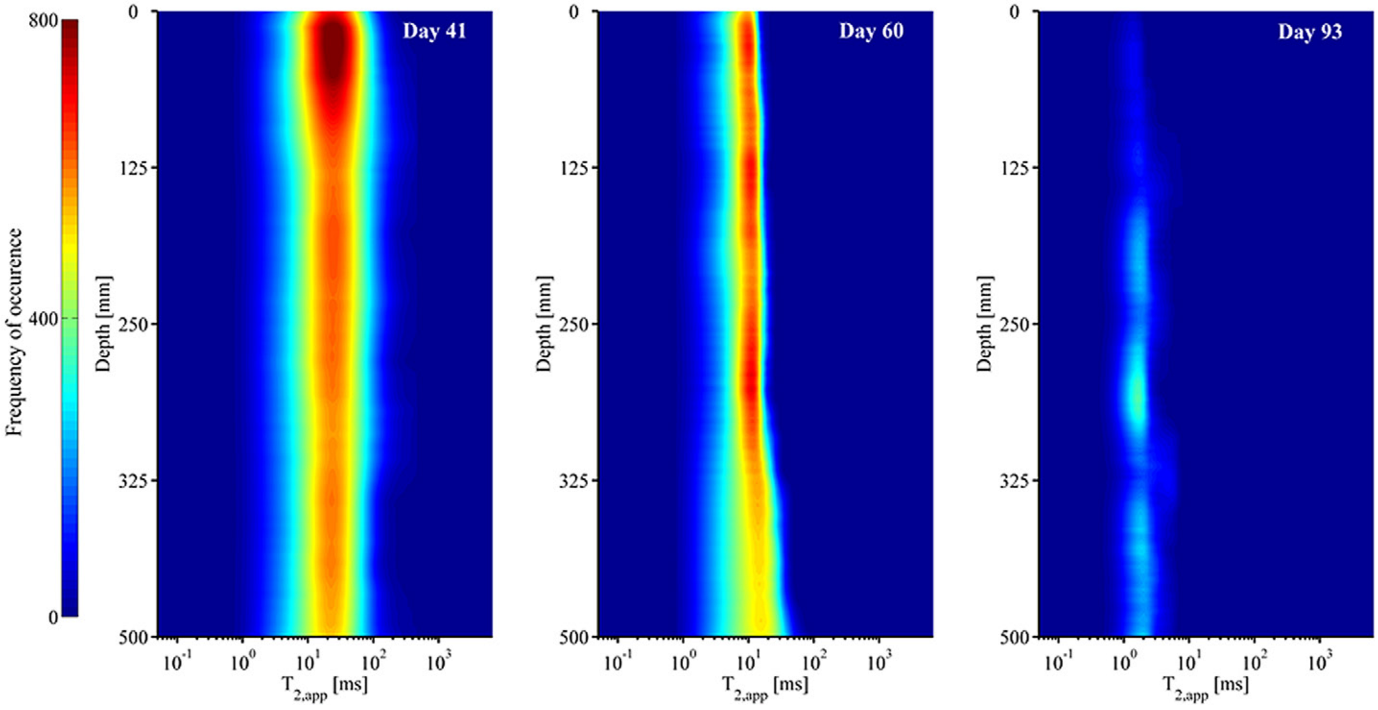

Fig. 8. The apparent transversal relaxation time distribution ($T_{2,\mathrm{app}}$) spectra as a function of drying time of the 500-mm sandy loam column monitored at 2.2 MHz by means of spin echo single-point imaging with a resolution of 2 mm per data point.

where the bimodality was covered by the broad bulk distribution curve. The bimodality for both soils can be explained with the formation of clay and silt microaggregates and clay coating of sand particles. With ongoing evaporation, the overall signal amplitude decreased, and the $T_{2,\mathrm{app}}$ and T_1 distributions shifted toward faster relaxation times. Because water is constantly withdrawn from the soil, the initially bimodal $T_{2,\mathrm{app}}$ distribution vanished. Water now becomes located in subsequently smaller pores, which causes the shift to faster relaxation times in both relaxation time distributions. The differences in the T_1 and $T_{2,\mathrm{app}}$ relaxation time spectra between both soil types were caused by the difference in pore size distribution and the soil composition. Because $T_{2,\mathrm{app}}$ is linked to the pore size, the sandy loam possesses larger $T_{2,\mathrm{app}}$ compared with the silt loam (Stingaciu et al., 2010). The desaturation coefficient (α) is related to n (Ng and Menzies, 2007) and increases with sand content. Therefore, the differences in n and α of both soil types are influenced by the moisture depletion at the onset of S2. At this stage of drying, the smallest accessible pores are emptied, causing a shift to fast $T_{2,\mathrm{app}}$ relaxation times where a MR signal is detectable at the secondary evaporation front. The spatially resolved $T_{2,\mathrm{app}}$ relaxation time spectra (Eq. [4]) therefore allow us to determine the position of the secondary evaporation front and thus the extent of the dry surface layer for both 60-mm columns (Fig. 7, white arrow). The signal shifts to faster relaxation times (moisture in smaller pores) toward the secondary evaporation plane and vanishes at the secondary evaporation plane (no detectable MR signal). For both soils, the CPMG (whole column) and SE-SPI (spatially resolved) methods yielded identical results. For the SE-SPI method, the position of the front deduced from the $T_{2,\mathrm{app}}$ relaxation time spectra was in good agreement with the measured and simulated moisture profiles (Fig. 2d and 3d). The moisture gradient attached to the secondary evaporation front shows a narrowed $T_{2,\mathrm{app}}$ distribution and a decrease in the overall signal amplitude. Even if the $T_{2,\mathrm{app}}$ signal amplitude significantly decreased toward the surface of the 500-mm sandy loam column, a secondary evaporation front could not clearly be distinguished. This is due to the extent of the front of 10 mm, which is smaller than the spatial resolution of the measurement. In this region, the water content of the boundary layer (relative humidity) is still in balance with the vapor inside the dry layer, leading to a detectable signal in the SE-SPI measurements.

Summary and Conclusions

In this study, we monitored the evaporative drying over time of three different soil columns by means of different MR methods to compare the effective saturation profiles of each column to the one-dimensional Richards approach and a more complex fully coupled liquid water, vapor, and heat flow model. The results indicate that different ^{1}H-MR methods, such as the $T_{2,\mathrm{app}}$ distribution in combination with the signal amplitude, are feasible tools to monitor the drying process of natural soils at the laboratory scale. Distinct evaporation stages (S1 and S2) along the development of a dry topmost layer were monitored for a sandy loam and a silt loam. The numerical coupled model approach showed that there is a need to consider heat and vapor flow instead of solely water flow, as it is for the Richards equation. The latter can lead to overestimations in the volumetric water content. On the other hand, there is a good agreement between the results of the coupled model and the MR data, particularly down to lower moisture contents. Nevertheless, because all soil parameters were derived independently by means of the HYPROP evaporation method, the achieved parameters might be biased (Schindler et al., 2010b) due to, for example, differences in packing. This might also have affected the modeling results. Because this study's outcome is based on one replicate for each type of soil and column length, it is considered as a study toward MR applications to investigate water flow in soils with dry surface layers. Therefore, our measurements, in combination with the coupled model results, can be seen as a proof of principle where the MR methods may be applicable on mobile MR devices, such as the NMR MOUSE, to monitor moisture content and relaxation time spectra as a function of space and time in the top layer of soils directly in the field. This approach holds the potential to strengthen the links between laboratory-scale investigations, field-scale measurements, and theoretical calculations (Costabel and Günther, 2014; de Pasquale and Mohnke, 2014; Rezaei et al., 2016; Vereecken et al., 2016; Wang, 2015).

Acknowledgments

This work was supported by Deutsche Forschungsgesellschaft (DFG, SFB/TR 32 "Patterns in Soil–Vegetation–Atmosphere Systems: Monitoring, Modelling and Data Assimilation"). B. Balcom thanks NSERC of Canada for a Discovery Grant and the Canada Chairs program for a research chair in MRI of materials, and S. Merz thanks Josée Owen from the Potato Research Centre in Fredericton (New Brunswick, Canada) for providing the soil material.

References

Abragam, A. 1961. The principles of nuclear magnetism. Oxford Univ. Press, Oxford, UK.

Andreas, E.L. 2005. Handbook of physical constants and functions for use in atmospheric boundary layer studies. Cold Regions Res. Eng. Lab., Hanover, NH. doi:10.21236/ADA440352

Andreev, S.V., and B.K. Martens. 1960. Soil moisture determination by the method of nuclear magnetic resonance. Soviet Soil Sci. 10:1129–1133.

Assouline, S., S.W. Tyler, J.S. Selker, I. Lunati, C.W. Higgins, and M.B. Parlange. 2013. Evaporation from a shallow water table: Diurnal dynamics of water and heat at the surface of drying sand. Water Resour. Res. 49:4022–4034. doi:10.1002/wrcr.20293

Barrie, P.J. 2000. Characterization of porous media using NMR methods. In: G.A. Webb, editor, Annual reports on NMR spectroscopy. Academic Press, Burlington, MA. p. 265–316. doi:10.1016/S0066-4103(00)41011-2

Ben Neriah, A., S. Assouline, U. Shavit, and N. Weisbrod. 2014. Impact of ambient conditions on evaporation from porous media. Water Resour. Res. 50:6696–6712. doi:10.1002/2014WR015523

Bernstein, M., K. King, and X. Zhou. 2004. Handbook of MRI pulse sequences. Academic Press, Burlington, MA.

Bittelli, M., F. Ventura, G.S. Campbell, R.L. Snyder, F. Gallegati, and P.R. Pisa. 2008. Coupling of heat, water vapor, and liquid water fluxes to compute evaporation in bare soils. J. Hydrol. 362:191–205. doi:10.1016/j.jhydrol.2008.08.014

Cameron, K.C., and G.D. Buchan. 2005. Porosity and pore size distribution. In: R. Lal, editor, Encyclopedia of soil science. 2nd ed. CRC Press, Boca Raton, FL. doi:10.1201/NOE0849338304.ch284

Casanova, F. 2011. Single-sided NMR. Springer, Berlin. doi:10.1007/978-3-642-16307-4

Cass, A., G.S. Campbell, and T.L. Jones. 1984. Enhancement of thermal water vapor diffusion in soil. Soil Sci. Soc. Am. J. 48:25–32. doi:10.2136/sssaj1984.03615995004800010005x

Chung, S.-O., and R. Horton. 1987. Soil heat and water flow with a partial surface mulch. Water Resour. Res. 23:2175–2186. doi:10.1029/WR023i012p02175

Coates, G.R., L. Xiao, and M.G. Prammer. 1999. NMR logging: Principles and applications. Haliburton Energy Serv., Houston, TX.

Costabel, S., and T. Günther. 2014. Noninvasive estimation of water retention parameters by observing the capillary fringe with magnetic resonance sounding. Vadose Zone J. 13(6). doi:10.2136/vzj2013.09.0163 de Pasquale, G., and O. Mohnke. 2014. Numerical study of prepolarized surface nuclear magnetic resonance in the vadose zone. Vadose Zone J. 13(11). doi:10.2136/vzj2014.06.0069

Dimitrov, M., J. Vanderborght, K.G. Kostov, B. Debecker, P. Schulze Lammers, L. Damerow, and H. Vereecken. 2015. Soil hydraulic parameters of bare soil plots with different soil structure inversely derived from L-band brightness temperatures. Vadose Zone J. 14(8). doi:10.2136/vzj2014.09.0133

Dunn, K.J., D.J. Bergman, and G.A. LaTorraca. 2002. Nuclear magnetic resonance: Petrophysical and logging applications. Elsevier, New York.

Duschl, M., P. Galvosas, T.I. Brox, A. Pohlmeier, and H. Vereecken. 2015. In situ determination of surface relaxivities for unconsolidated sediments. Water Resour. Res. 51:6549–6563. doi:10.1002/2014WR016574

Fetzer, T., J. Vanderborght, K. Mosthaf, K.M. Smits, and R. Helmig. 2017. Heat and water transport in soils and across the soil–atmosphere interface: 2. Numerical analysis. Water Resour. Res. 53:1080–1100. doi:10.1002/2016WR019983

Haber-Pohlmeier, S., S. Stapf, and A. Pohlmeier. 2014. NMR fast field cycling relaxometry of unsaturated soils. Appl. Magn. Reson. 45:1099–1115. doi:10.1007/s00723-014-0599-2

Han, J., and Z. Zhou. 2013. Dynamics of soil water evaporation during soil drying: Laboratory experiment and numerical analysis. Sci. World J. 2013:240280. doi:10.1155/2013/240280

Heitman, J.L., X. Xiao, R. Horton, and T.J. Sauer. 2008. Sensible heat measurements indicating depth and magnitude of subsurface soil water evaporation. Water Resour. Res. 44:W00D05. doi:10.1029/2008WR006961

Jaeger, F., S. Bowe, H. Van As, and G.E. Schaumann. 2009. Evaluation of ^{1}H NMR relaxometry for the assessment of pore-size distribution in soil samples. Eur. J. Soil Sci. 60:1052–1064. doi:10.1111/j.1365-2389.2009.01192.x

Jassal, R.S., M.D. Novak, and T.A. Black. 2003. Effect of surface layer thickness on simultaneous transport of heat and water in a bare soil and its implications for land surface schemes. Atmos.-Ocean 41:259–272. doi:10.3137/ao.410401

Kleinberg, R.L., S.A. Farooqui, and M.A. Horsfield. 1993. T_1/T_2 ratio and frequency dependence of NMR relaxation in porous sedimentary rocks. J. Colloid Interface Sci. 158:195–198. doi:10.1006/jcis.1993.1247

Kleinberg, R.L., and J.A. Jackson. 2001. An introduction to the history of NMR well logging. Concepts Magn. Reson. 13:340–342. doi:10.1002/cmr.1018

Koptyug, I.V. 2012. MRI of mass transport in porous media: Drying and sorption processes. Prog. Nucl. Magn. Reson. Spectrosc. 65:1–65. doi:10.1016/j.pnmrs.2011.12.001

Korb, J.P. 2011. Nuclear magnetic relaxation of liquids in porous media. New J. Phys. 13:035016. doi:10.1088/1367-2630/13/3/035016

Krause, P., D.P. Boyle, and F. Bäse. 2005. Comparison of different efficiency criteria for hydrological model assessment. Adv. Geosci. 5:89–97. doi:10.5194/adgeo-5-89-2005

Laurindo, J.B., and M. Prat. 1998. Numerical and experimental network study of evaporation in capillary porous media: Drying rates. Chem. Eng. Sci. 53:2257–2269. doi:10.1016/S0009-2509(97)00348-5

Legates, D.R., and G.J. McCabe. 1999. Evaluating the use of "goodness-of-fit" measures in hydrologic and hydroclimatic model validation. Water Resour. Res. 35:233–241. doi:10.1029/1998WR900018

Lehmann, P., S. Assouline, and D. Or. 2008. Characteristic lengths affecting evaporative drying of porous media. Phys. Rev. E 77:056309. doi:10.1103/PhysRevE.77.056309

Liu, B.C., W. Liu, and S.W. Peng. 2005. Study of heat and moisture transfer in soil with a dry surface layer. Int. J. Heat Mass Transfer 48:4579–4589. doi:10.1016/j.ijheatmasstransfer.2005.06.004

Mastikhin, I.V., and B.J. Balcom. 2012. Centric SPRITE MRI of biomaterials with short T_2. John Wiley & Sons, Chichester, UK.

McIntosh, L.P. 2013. CPMG. In: G.K. Roberts, editor, Encyclopedia of biophysics. Springer, Berlin. p. 386. doi:10.1007/978-3-642-16712-6_320

Merz, S., A. Pohlmeier, B.J. Balcom, R. Enjilela, and H. Vereecken. 2015a. Drying of a natural soil under evaporative conditions: A comparison of different magnetic resonance methods. Appl. Magn. Reson. 47:121–138. doi:10.1007/s00723-015-0736-6

Merz, S., A. Pohlmeier, J. Vanderborght, D. van Dusschoten, and H. Vereecken. 2014. Moisture profiles of the upper soil layer during evaporation monitored by NMR. Water Resour. Res. 50(6):5184–5195. doi:10.1002/2013WR014809

Merz, S., A. Pohlmeier, J. Vanderborght, D. van Dusschoten, and H. Vereecken. 2015b. Transition of stage I to stage II evaporation regime in the topmost soil: High-resolution NMR imaging, profiling and numerical simulation. Microporous Mesoporous Mater. 205:3–6. doi:10.1016/j.micromeso.2014.10.035

Moghadas, D., K.Z. Jadoon, J. Vanderborght, S. Lambot, and H. Vereecken. 2013. Effects of near surface soil moisture profiles during evaporation on far-field ground-penetrating radar data: A numerical study. Vadose Zone J. 12(2). doi:10.2136/vzj2012.0138

Moghadas, D., K.Z. Jadoon, J. Vanderborght, S. Lambot, and H. Vereecken. 2014. Estimation of the near surface soil water content during evaporation using air-launched ground-penetrating radar. Near Surf. Geophys. 12:623–633. doi:10.3997/1873-0604.2014017

Mualem, Y. 1976. A new model for predicting the hydraulic conductivity of unsaturated porous media. Water Resour. Res. 12:513–522. doi:10.1029/WR012i003p00513

Muir, C.E., and B.J. Balcom. 2012. Pure phase encode magnetic resonance imaging of fluids in porous media. In: A.W. Graham, editor, Annual reports on NMR spectroscopy. Academic Press, Burlington, MA. p. 81–113. doi:10.1016/B978-0-12-397020-6.00002-7

Nash, J.E., and J.V. Sutcliffe. 1970. River flow forecasting through conceptual models: I. A discussion of principles. J. Hydrol. 10:282–290. doi:10.1016/0022-1694(70)90255-6

Nestle, N., R. Morris, and T. Baumann. 2007. Environmental NMR: Magnetic resonance imaging. eMagRes 2(4). doi:10.1002/9780470034590.emrstm1349

Ng, C.W., and B. Menzies. 2007. Advanced unsaturated soil mechanics and engineering. CRC Press, Boca Raton, FL.

Nimmo, J.R., and E.E. Miller. 1986. The temperature dependence of isothermal moisture vs. potential characteristics of soils. Soil Sci. Soc. Am. J. 50:1105–1113. doi:10.2136/sssaj1986.03615995005000050004x

Novak, M.D. 2010. Dynamics of the near-surface evaporation zone and corresponding effects on the surface energy balance of a drying bare soil. Agric. For. Meteorol. 150:1358–1365. doi:10.1016/j.agrformet.2010.06.005

Oki, T., and S. Kanae. 2006. Global hydrological cycles and world water resources. Science 313:1068–1072. doi:10.1126/science.1128845

Or, D., P. Lehmann, E. Shahraeeni, and N. Shokri. 2013. Advances in soil evaporation physics: A review. Vadose Zone J. 12(4). doi:10.2136/vzj2012.0163

Peters, A., and W. Durner. 2008. Simplified evaporation method for determining soil hydraulic properties. J. Hydrol. 356:147–162. doi:10.1016/j.jhydrol.2008.04.016

Petrov, O.V., G. Ersland, and B.J. Balcom. 2011. T_2 distribution mapping profiles with phase-encode MRI. J. Magn. Reson. 209:39–46. doi:10.1016/j.jmr.2010.12.006

Philip, J.R., and D.A. De Vries. 1957. Moisture movement in porous materials under temperature gradients. Eos Trans. Am. Geophys. Union 38:222–232. doi:10.1029/TR038i002p00222

Pomerantz, A.E., P. Tilke, and Y.-Q. Song. 2008. Inverting MRI measurements to heterogeneity spectra. J. Magn. Reson. 193:243–250. doi:10.1016/j.jmr.2008.05.014

Qiu, G.Y., and J. Ben-Asher. 2010. Experimental determination of soil evaporation stages with soil surface temperature. Soil Sci. Soc. Am. J. 74:13–22. doi:10.2136/sssaj2008.0135

Rezaei, M., P. Seuntjens, R. Shahidi, I. Joris, W. Boënne, B. Al-Barri, and W. Cornelis. 2016. The relevance of in-situ and laboratory characterization of sandy soil hydraulic properties for soil water simulations. J. Hydrol. 534:251–265. doi:10.1016/j.jhydrol.2015.12.062

Richards, L.A. 1931. Capillary conduction of liquids through porous mediums. Physics 1:318–333. doi:10.1063/1.1745010

Robinson, D.A., C.S. Campbell, J.W. Hopmans, B.K. Hornbuckle, S.B. Jones, R. Knight, et al. 2008. Soil moisture measurement for ecological and hydrological watershed-scale observatories: A review. Vadose Zone J. 7:358–389. doi:10.2136/vzj2007.0143

Rogowski, A.S. 1971. Watershed physics: Model of the soil moisture characteristic. Water Resour. Res. 7:1575–1582. doi:10.1029/WR007i006p01575

Rothfuss, Y., S. Merz, J. Vanderborght, N. Hermes, A. Weuthen, A. Pohlmeier, et al. 2015. Long-term and high-frequency non-destructive monitoring of water stable isotope profiles in an evaporating soil column. Hydrol. Earth Syst. Sci. 19:4067–4080. doi:10.5194/hess-19-4067-2015

Saito, H., J. Šimůnek, and B.P. Mohanty. 2006. Numerical analysis of coupled water, vapor, and heat transport in the vadose zone. Vadose Zone J. 5:784–800. doi:10.2136/vzj2006.0007

Sakai, M., N. Toride, and J. Šimůnek. 2009. Water and vapor movement with condensation and evaporation in a sandy column. Soil Sci. Soc. Am. J. 73:707–717. doi:10.2136/sssaj2008.0094

Schaap, M.G., F.J. Leij, and M.Th. van Genuchten. 2001. Rosetta: A computer program for estimating soil hydraulic parameters with hierarchical pedotransfer functions. J. Hydrol. 251:163–176. doi:10.1016/S0022-1694(01)00466-8

Scherer, G.W. 1990. Theory of drying. J. Am. Ceram. Soc. 73:3–14. doi:10.1111/j.1151-2916.1990.tb05082.x

Schindler, U., W. Durner, G. von Unold, L. Mueller, and R. Wieland. 2010a. The evaporation method: Extending the measurement range of soil hydraulic properties using the air-entry pressure of the ceramic cup. J. Plant Nutr. Soil Sci. 173:563–572. doi:10.1002/jpln.200900201

Schindler, U., W. Durner, G. von Unold, L. Mueller, and R. Wieland. 2010b. The evaporation method: Extending the measurement range of soil hydraulic properties using the air-entry pressure of the ceramic cup. J. Plant Nutr. Soil Sci. 173:563–572. doi:10.1002/jpln.200900201

Schlünder, E.U. 2004. Drying of porous material during the constant and the falling rate period: A critical review of existing hypotheses. Dry. Technol. 22:1517–1532. doi:10.1081/DRT-120038738

Shahraeeni, E., P. Lehmann, and D. Or. 2012. Coupling of evaporative fluxes from drying porous surfaces with air boundary layer: Characteristics of evaporation from discrete pores. Water Resour. Res. 48:W09525. doi:10.1029/2012WR011857

Shokri, N., P. Lehmann, P. Vontobel, and D. Or. Vontobel, and D. Or. 2008. Drying front and water content dynamics during evaporation from sand delineated by neutron radiography. Water Resour. Res. 44:W06418. doi:10.1029/2007WR006385

Šimůnek, J., M.Th. van Genuchten, and M. Šejna. 2008. Modeling subsurface water flow and solute transport with HYDRUS and related numerical software packages. In: P. Garcia-Navarro and E. Playán, editors, Numerical modelling of hydrodynamics for water resources. Taylor & Francis, London. p. 95–114.

Stingaciu, L.R., L. Weihermüller, S. Haber-Pohlmeier, S. Stapf, H. Vereecken, and A. Pohlmeier. 2010. Determination of pore size distribution and hydraulic properties using nuclear magnetic resonance relaxometry: A comparative study of laboratory methods. Water Resour. Res. 46:W11510. doi:10.1029/2009WR008686

Teng, J.D., N. Yasufuku, S. Zhang, and Y. He. 2016. Modelling water content redistribution during evaporation from sandy soil in the presence of water table. Comput. Geotech. 75:210–224. doi:10.1016/j.compgeo.2016.02.009

Tran, D.T.Q., D.G. Fredlund, and D.H. Chan. 2015. Improvements to the calculation of actual evaporation from bare soil surfaces. Can. Geotech. J. 53:118–133. doi:10.1139/cgj-2014-0512

Trenberth, K.E., J.T. Fasullo, and J. Kiehl. 2009. Earth's global energy budget. Bull. Am. Meteorol. Soc. 90:311–323. doi:10.1175/2008BAMS2634.1

Vanderborght, J., T. Fetzer, K. Mosthaf, K.M. Smits, and R. Helmig. 2017. Heat and water transport in soils and across the soil–atmosphere interface: 1. Theory and different model concepts. Water Resour. Res. 53:1057–1079. doi:10.1002/2016WR019982

Vanderborght, J., A. Graf, C. Steenpass, B. Scharnagl, N. Prolingheuer, M. Herbst, et al. 2010. Within-field variability of bare soil evaporation derived from eddy covariance measurements. Vadose Zone J. 9:943–954. doi:10.2136/vzj2009.0159

van Genuchten, M.Th. 1980. A closed-form equation for predicting the hydraulic conductivity of unsaturated soils. Soil Sci. Soc. Am. J. 44:892–898. doi:10.2136/sssaj1980.03615995004400050002x

van Keulen, H., and D. Hillel. 1974. A simulation study of the drying-front phenomenon. Soil Sci. 118:270–273. doi:10.1097/00010694-197410000-00008

Vereecken, H., A. Schnepf, J.W. Hopmans, M. Javaux, D. Or, T. Roose, et al. 2016. Modeling soil processes: Review, key challenges, and new perspectives. Vadose Zone J. 15(5). doi:10.2136/vzj2015.09.0131

Wang, X. 2015. Vapor flow resistance of dry soil layer to soil water evaporation in arid environment: An overview. Water 7:4552–4574. doi:10.3390/w7084552

Watson, A.T., and C.T.P. Chang. 1997. Characterizing porous media with NMR methods. Prog. Nucl. Magn. Reson. Spectrosc. 31:343–386. doi:10.1016/S0079-6565(97)00053-8

Wythers, K.R., W.K. Lauenroth, and J.M. Paruelo. 1999. Bare-soil evaporation under semiarid field conditions. Soil Sci. Soc. Am. J. 63:1341–1349. doi:10.2136/sssaj1999.6351341x

Yiotis, A.G., I.N. Tsimpanogiannis, A.K. Stubos, and Y.C. Yortsos. 2007. Coupling between external and internal mass transfer during drying of a porous medium. Water Resour. Res. 43:W06403.

Zeng, Y. 2013. Coupled dynamics in soil. Springer, Berlin. doi:10.1007/978-3-642-34073-4